

TIDAL DISRUPTION OF A STAR BY A BLACK HOLE : OBSERVATIONAL SIGNATURE

TAMARA BOGDANOVIĆ¹, MICHAEL ERACLEOUS, SUVRATH MAHADEVAN, STEINN SIGURDSSON¹, AND
PABLO LAGUNA¹

Department of Astronomy & Astrophysics, The Pennsylvania State University, University Park, PA 16802
Center Preprint Number: CGPG-03/9-3

ABSTRACT

We have modeled the time-variable profiles of the H α emission line from the non-axisymmetric disk and debris tail created in the tidal disruption of a solar-type star by a $10^6 M_{\odot}$ black hole. Two tidal disruption event simulations were carried out using a three dimensional relativistic smooth-particle hydrodynamic code, to describe the early evolution of the debris during the first fifty to ninety days. We have calculated the physical conditions and radiative processes in the debris using the photoionization code CLOUDY. We model the emission line profiles in the period immediately after the accretion rate onto the black hole became significant. We find that the line profiles at these very early stages of the evolution of the post-disruption debris do not resemble the double peaked profiles expected from a rotating disk since the debris has not yet settled into such a stable structure. As a result of the uneven distribution of the debris and the existence of a “tidal tail” (the stream of returning debris), the line profiles depend sensitively on the orientation of the tail relative to the line of sight. Moreover, the predicted line profiles vary on fairly short time scales (of order hours to days). Given the accretion rate onto the black hole we also model the H α light curve from the debris and the evolution of the H α line profiles in time.

Subject headings: black hole physics—galaxies: nuclei—line: profiles

1. INTRODUCTION

1.1. *Tidal Disruption of a Star by a Black Hole and Related Issues*

A star in an orbit around a massive black hole can get tidally disrupted during its close passage by the black hole. After several orbital periods the debris from the disrupted star settles into an accretion disk and gradually falls into the black hole (Rees 1988; Cannizzo, Lee & Goodman 1990; Syer & Clarke 1992; Loeb & Ulmer 1997). As material gets swallowed by the black hole intense UV or soft-X ray radiation is expected to emerge from the innermost rings of the accretion disk (Frank & Rees 1976; Lightman & Shapiro 1977; Frank 1978; Phinney 1989; Sembay & West 1993; Magorrian & Tremaine 1999; Syer & Ulmer 1999). For black hole masses $M_{bh} < 10^7 M_{\odot}$, tidal disruption theory predicts flares with luminosities of the order of the Eddington luminosity with durations of the order of months, and with spectra that peak in the UV/X-ray domain band (Rees 1988; Evans & Kochanek 1989; Ulmer 1999; Kim et al. 1999; Gezari et al. 2002). High-energy flares from the central source illuminate the debris, the photons get absorbed, and some are re-emitted in the optical part of the spectrum (i.e. the light is “reprocessed”). One of the spectral lines in which this phenomenon can be observed is the Balmer series H α line ($\lambda_{rest} = 6563 \text{ \AA}$).

The disruption of a star begins when the star approaches the tidal radius, $r_t \simeq r_{\star} (M_{bh}/M_{\star})^{1/3}$, the point where the surface gravity of the star equals the tidal acceleration from the black hole across the diameter of the star (r_{\star} and M_{\star} are the radius and mass of the star and M_{bh} is the mass of the black hole). A $10^6 M_{\odot}$ black hole is often used as a prototypical example in tidal disruption calculations. This choice is motivated by the criterion for a

solar-type star to be disrupted before it crosses the black hole horizon (i.e. the Schwarzschild radius, r_s) in order for emission to be observable. For supermassive black holes with $M_{bh} > 10^8 M_{\odot}$, $r_s > r_t$ and the star falls into the black hole before it gets disrupted.

The tidal disruption process has been the subject of many simulations (Carter & Luminet 1982, 1983; Bicknell & Gingold 1983; Evans & Kochanek 1989; Khokhlov, Novikov, & Pethick 1993; Laguna et al. 1993b; Frolov et al. 1994; Marck, Lioure, & Bonazzola 1996; Deiner et al. 1997; Ayal, Livio, & Piran 2000; Ivanov & Novikov 2001; Ivanov, Chernyakova, & Novikov 2003). It has been shown that tidal processes in the vicinity of a massive black hole could lead to tidal capture, tidal heating and tidal spin-up of a star (Novikov, Pethick, & Polnarev 1992; Alexander & Kumar 2001; Alexander & Hopman 2003; Alexander & Morris 2003), and in some cases ultimately to the explosion of the star. Such explosions, as well as accretion of post-disruption debris, should manifest themselves as luminous flares from the centers of galaxies (Carter & Luminet 1982; Rees 1988). Stars close to a black hole may experience mixing or may eject some of their mass (Alexander 2001). As a consequence, stellar populations in nuclear clusters are expected to be somewhat unusual in comparison with populations whose evolution was not affected by a massive black hole (Alexander & Livio 2001; Di Stefano et al. 2001). This has important implications for observations of stellar cluster in the center of our Galaxy (Ghez et al. 2000; Schöedl et al. 2002; Eckart, Ott, & Genzel 1999; Figer et al. 2000; Gezari et al. 2003) where high concentration of otherwise rare blue He supergiants has been observed (Krabbe et al. 1991; Najarro et al. 1994).

The tidal disruption and accretion of stars can fuel black holes in the centers of galaxies (Hills 1975; Dun-

¹ also member of Center for Gravitational Wave Physics

can & Shapiro 1982; David, Durisen, & Cohn 1987a,b; Murphy, Cohn, & Durisen 1991; Freitag & Benz 2002; Yu 2003) and its contribution to nuclear activity in galaxies and the growth of the black hole mass depends on the rate of disruption events in a galaxy. The predicted tidal disruption rate in a typical inactive galaxy is 10^{-4} – 10^{-5} yr $^{-1}$ (Magorrian & Tremaine 1999; Alexander 2001). This value is consistent with the rate of UV/X-ray outbursts observed with *ROSAT* from inactive nuclei selected as tidal disruption candidates (Donley et al. 2002). The rate of tidal disruptions in active and more luminous nuclei is estimated to be lower, with the lowest value of 10^{-9} yr $^{-1}$, for galaxies with the most massive black holes. This may occur partly because massive central black holes ($M_{bh} > 10^8 M_{\odot}$) swallow stars promptly, without disruption, and partly because stars are less centrally concentrated in these galaxies (Magorrian & Tremaine 1999). The observed UV/X-ray flaring rate in these galaxies is about 9×10^{-4} galaxy $^{-1}$ yr $^{-1}$ (Donley et al. 2002) suggesting that in such nuclei, outbursts may be due to another mechanism, such as accretion-disk instabilities (Siemiginowska, Czerny, & Kostyunin 1996; Burderi, King, & Szuszkiewicz 1998).

The tidal encounter of a compact star with a black hole can also result in emission of gravitational waves, which may be observable with upcoming instruments. More specifically, compact stars (helium stars, white dwarfs, neutron stars, and stellar-mass black holes) which can withstand large tidal forces without being disrupted, may get captured in relativistic orbits around a supermassive black hole. Due to the in-spiral and decay of the orbit those objects are expected to emit the peak of their gravitational wave power in the LISA frequency band (Hils & Bender 1995; Sigurdsson & Rees 1997; Freitag 2001). It has been recently suggested by Freitag (2003) that very-low mass main sequence stars (MSSs; $M \ll 1 M_{\odot}$) may contribute to events detected by LISA, which was not previously expected for capture of these objects by a supermassive black hole. Although MSSs produce a relatively weak gravitational signal during the in-spiral, compared to compact objects, their detection in the Galactic center is more likely because such stars have a predicted close-encounter rate that is an order of magnitude higher than that of white dwarfs (WDs), and about two or more orders of magnitude higher than that of neutron stars (NSs) and stellar-mass black holes (BHs). These compact MSSs are expected to produce a strong enough signal to allow for 0.5–2 detections from our Galactic center, with a signal-to-noise ratio of 10 or higher, for a LISA mission duration of one year (Freitag 2003). Moreover, MSSs are expected to be disrupted relatively early during the in-spiral, giving rise to possibly detectable electromagnetic flares. The sudden appearance of an electromagnetic counterpart to a transient gravitational wave source, expected in the case of MSSs and helium stars, could allow identification of the progenitor. In the case of a tidal disruption event in another galaxy, the coincidence of an electromagnetic flare and a gravitational wave signal would provide an indication that the event occurred at the very nucleus of the galaxy, and possibly allow the measurement of the redshift. More compact objects which can spiral in without being disrupted (such as WDs, NSs, and BHs) are ex-

pected to produce stronger gravitational wave signatures and weaker or no electromagnetic flares, with the exception of white dwarfs in which tidal interaction may trigger thermonuclear explosion (García-Senz, Bravo & Woosley 1999).

1.2. *Observational Motivation: Transient Emission Lines in Inactive Galaxies and LINERs*

In view of the above theoretical considerations, it is necessary to make predictions of the likely observational signatures of a tidal disruption event. The prompt UV/soft-X-ray flash that is expected to accompany the disruption does provide strong evidence for such an event and has in fact been detected in a number of galaxies with *ROSAT* and *HST* (Brandt, Pounds & Fink 1995; Grupe et al. 1995a,b; Donley et al. 2002; Bade, Komossa, & Dahlem 1996; Komossa & Greiner 1999; Greiner et al. 2000; Grupe, Thomas, & Leighly 1999; Renzini et al. 1995; Li, Narayan, & Menou 2002). However, the duration of this flash is short enough that it can easily be missed. Aftereffects with a longer duration, such as line emission from the debris, have a better chance of being detected. If the appearance of emission lines just after an X-ray flare could be detected from the same object it could be used to identify the tidal disruption in the early phase and would provide strong support for the overall picture, but such cases are rare (see Cappellari et al. 1999; Gezari et al. 2003).

A set of tantalizing observations in the past decade show that several LINERs (low-ionization nuclear emission regions; Heckman 1980) have transient Balmer emission lines, which are often double-peaked; examples include NGC 1097 (Storchi-Bergmann, Baldwin & Wilson 1993), M81 (Bower 2000), NGC 4450 (Ho et al. 2000), NGC 4203 (Shields et al. 2000) and NGC 3065 (Eracleous & Halpern 2001). Such line profiles are characteristic of rotating disks and resemble the persistent double-peaked Balmer lines found in about 10–20% of broad-line radio galaxies and about 3% of all active galaxies (e.g., Eracleous & Halpern 1994, 2003; Strateva et al. 2003). Their abrupt appearance in LINERs led to suggestions that this transient event was related to the tidal disruption of a star by a supermassive, nuclear black hole (Eracleous et al. 1995; Storchi-Bergmann et al. 1995) or a change in the structure of the accretion disk associated with a change in accretion rate (Storchi-Bergmann et al. 1997).

To investigate the possibility of line emission from the post-disruption debris and to evaluate the suggestion that the transient double-peaked lines of LINERs are related to tidal disruption events, we have undertaken a calculation of the strength and profile of the H α line emitted from the debris. In §2, We describe two SPH (Smoothed Particle Hydrodynamics) simulations of tidal disruption on which we base our further calculation of the line properties. Our line profile calculation follows the method used for line profiles emitted by relativistic, Keplerian disks and is described in §3. In §4 we present the resulting line profiles and in §5 we discuss the physical conditions in the debris and the approximations used. In §6 we summarize our conclusions and consider future prospects.

Tidal disruption simulations were carried out with a three dimensional relativistic SPH code in order to study the dynamical evolution of the post-disruption debris. The SPH code used provides a description of relativistic fluid flows in a static curved spacetime geometry (Laguna et al. 1993a,b). We use it to simulate the tidal disruption of a star in the potential of a Schwarzschild black hole.

The main sequence star is modeled as a polytrope with index $\Gamma = 5/3$. The density profile of the pre-disruption star is determined by the Lane-Emden equations. The star is initially placed on a parabolic orbit at a distance of $700 r_g$ from the black hole where $r_g = r_s/2 = GM/c^2 = M$ is the gravitational radius and M is the mass of the black hole. Hereafter we use units in which $G \equiv c \equiv 1$, where G is the gravitational constant and c is the speed of the light and we adopt $r_g = M$ as a natural unit of length. The gravitational radius of a $10^6 M_\odot$ black hole is $r_g = 1.48 \times 10^{11}$ cm = 4.92 light seconds and the dynamical time at a given radius is $\tau_{dyn} \sim (r^3/GM)^{1/2} = 4.92 (r/r_g)^{3/2}$ s.

The strength of the tidal encounter, is given by the ratio of tidal radius to pericentric distance, $\eta = r_t/r_p$. For the case of $1 M_\odot$ star and a $10^6 M_\odot$ black hole $r_t \simeq 47 r_g$. The two SPH simulations describe the tidal disruption for the case of mildly relativistic encounter, $\eta=1.2$. This value has been selected as a likely scenario for tidal disruption of a main sequence star. We do not investigate the strongly relativistic cases where tidal compression could lead to the explosion of a star, because such an explosion could introduce an uncertainty in the distribution of the debris mass over binding energy and consequently in the spatial distribution and kinematics of the debris.

The self gravity of the star is accounted for initially. Once the star gets disrupted the self-gravity becomes unimportant and the debris particles follow nearly Keplerian orbits. It can be shown for the case of the Keplerian potential that the rate of return of bound debris to the pericenter follows $dM/dt \propto t^{-5/3}$ (Rees 1988; Phinney 1989). This behavior of the debris return rate has been observed in our SPH simulations. Once bound debris starts to rain down on the black hole it is expected to cause the initial rapid rise in the emitted UV/X-ray light curve and steady decay with the power law index of $-5/3$ later on.

The two different simulations have 5,000 and 20,000 particles (hereafter 5k and 20k respectively) contributing equally to the mass of a $1 M_\odot$ star. The 5k SPH calculation follows the debris for 94 days in total. After 34 days significant accretion onto the black hole begins. Our investigation follows the evolution of the line profiles in the last 60 days. The 20k SPH simulation spans 53 days, during which the evolution of the line profiles was followed for the last 6 days (Table 1). Using both the 5k and 20k SPH simulations in the line profile modeling we take advantage of the longer time span in the former and better resolution achieved with the larger number of particles in the latter.

Figure 1 shows particle distribution maps after the second pericentric passage, at the beginning of the accretion phase and at the end of the 5k simulation. At the early stages of the tidal event most of the particles were located in the pronounced tidal tail. Sixty days later, about 20% of the particles are scattered from the tidal tail and form a quasi-spherical distribution, with most of its mass concentrated in the equatorial plane (Cannizzo et al. 1990; Loeb

& Ulmer 1997; Ulmer, Paczynski & Goodman 1998; Ulmer 1999; Menou & Quataert 2001). This is a consequence of the intersection of the leading part of the tidal stream with itself (Kochanek 1994; Lee, Kang, & Ryu 1996; Kim et al. 1999; Ayal et al. 2000). We refer to the spheroidal part of the debris as the halo and to its planar component as the disk. The remaining 79% of particles are still confined to the tail and 1% are accreted onto the black hole. There is a concern that some fraction of particles ($\sim \frac{\tau_{run}}{\tau_{dyn}} \sqrt{N}$, where τ_{run} and N are the total duration and total number of particles in the run) of the halo are an artifact of the SPH simulation. This can be due to the tendency of the SPH numerical method to preserve the constant number of neighbor particles for each particle during the calculation. In the regions with a small density of particles this leads to a “smoothing” over a large spatial range and it may introduce the scatter of particles from the debris plane to the halo. These particles cannot be distinguished from the population of particles scattered out of the debris plane by the intersection of the tidal tail with itself. We further discuss the implications of the spheroidal halo for the emission line profiles and total H α luminosity in §5.2.

The velocity distribution in the tail is “bimodal” where the central part of the tail exhibits very low radial velocities: particles on the near (right-hand) side of the tail “flow” towards the black hole, while particles on far (left-hand) side are moving in the opposite direction. This is a consequence of the energy distribution throughout the debris in the disruption process: after the initial disruption event 50% of the debris stays bound to the system and the other 50% is unbound. This effect has been predicted by theory in the case of stellar disruption after a single fly-by of the star (Rees 1988) and has been observed in tidal disruption simulations. The symmetry in the distribution of the debris over binding energy is a consequence of the spin-up of the star at the expense of orbital kinetic energy. The spin-up initially causes the development of a quadrupolar deformation. As the tidal interaction gets stronger the star starts to shed its mass since the material in the stellar bulge has reached the escape velocity at the star’s surface. One portion of the stellar debris ends up deeper in the potential well of the black hole, which causes further spread in binding energy of the debris. This effect determines which portion of the debris stays bound to the black hole Rees (1988). Following the second passage of the debris through pericenter approximately 66% of the mass is unbound, 33% remains bound and only about 1% is accreted by the black hole. The maximal approaching and receding velocities in the debris, with respect to the stationary observer positioned at infinity, are of order $10^{-2}c$. The dynamical evolution in the 20k run is the same, it is just followed over a shorter evolutionary time scale. Since the tidal tail includes a large fraction of bound and unbound particles in both simulations, its morphology and velocity field greatly influence the observed line profiles.

3. LINE PROFILE CALCULATION AND TIME DELAY OF REPROCESSED LIGHT

3.1. Calculation of Line Profiles

We follow the line profile calculations carried out by Chen & Halpern (1989) and Eracleous et al. (1995) to obtain the observed profile from a Keplerian, relativistic, thin

disk in the weak field approximation. The description of the debris as a flat, thin structure is justified by the fact that the height of the debris is three orders of magnitude less than its dimensions in the orbital plane. The main objective of the calculation is to obtain the final expression for the flux density in the observer's frame as a function of parameters defined in the reference frame of the debris. Figure 2 shows the coordinate system and the geometry of the debris. The observer is located on the positive z-axis, at a distance $d \rightarrow +\infty$ and above the orbital plane at $i = 30^\circ$ to the z' -axis. Since the calculation is presented in cited papers we just introduce its main steps and comment on its application to the case of tidal disruption debris.

The total emission-line flux received from the debris by an observer at infinity is given by an integral over the plane of the image produced at infinity, namely

$$F = \int d\nu \int \int d\Omega I_\nu \quad (1)$$

where ν , I_ν , and $d\Omega$ are the frequency, specific intensity and solid angle element measured in the frame of the image (i.e., of the observer). Using the impact parameter of rays at infinity, b , as a coordinate in the image plane and exploiting the Lorentz invariance of the quantity I_ν/ν^3 and the fact that the debris is confined to a plane, equation (1) can be transformed into an expression for the flux density (i.e., the line profile) in terms of coordinates and physical quantities in the source frame (see detailed derivation in Chen, Halpern, & Filippenko 1989, Chen & Halpern 1989, and Eracleous et al. 1995)

$$f_\nu = \int \int d\Omega I_\nu = \frac{M^2 \nu_0 \cos i}{d^2} \int_{\xi_{in}}^{\xi_{out}} \xi d\xi \int_0^{2\pi} d\phi' I_{\nu_e} D^3(\xi, \phi') \psi(\xi, \phi') \quad (2)$$

where the new polar coordinates in the debris plane are the dimensionless radius $\xi \equiv r/r_g$ and the azimuthal angle ϕ' . In practice, the integration is performed by summing over particles, assigning to each particle an emissivity according to its position, as derived from calculation with the code CLOUDY (Ferland 1996, see §4.1). The limits of integration describe the portion of the debris that emits the H α line, between radii ξ_{in} and ξ_{out} . The function $D(\xi, \phi')$, the ‘‘Doppler factor,’’ is determined by the phase space distribution of the emitting particles and the metric, and describes the effects of gravity and the motion of the emitting particles on the energies of the emitted photons. The function $\psi(\xi, \phi')$ is determined by the geometrical distribution of the emitting particles and the metric, and describes the effects of curved trajectories of light rays. In the special case where the debris is confined to a plane, these functions are given by

$$D = \frac{(1 - 2/\xi)^{1/2}}{\gamma} \left\{ 1 - \frac{\beta_{r'}}{1 - 2/\xi} [1 - (b/r)^2(1 - 2/\xi)]^{1/2} + \frac{\beta_{\phi'}}{(1 - \sin^2 i \cos^2 \phi')^{1/2}} \right\}^{-1}, \quad (3)$$

with γ the Lorentz factor, $\beta_{r'}$ and $\beta_{\phi'}$ the radial and azimuthal velocities of debris particles *in the source frame*, and

$$\psi(\xi, \phi') = 1 + \frac{1}{\xi} \left(\frac{1 - \sin i \cos \phi'}{1 + \sin i \cos \phi'} \right). \quad (4)$$

The above analytic expression for $\psi(\xi, \phi')$ has been derived in the weak field approximation and is accurate to order ξ^{-1} . This approximation is appropriate in our case because the portions of the debris that experience a strong gravitational field are also highly ionized and make a negligible contribution to the H α flux (see discussion in §5.1). The ratio b/r describes how rays emitted from the debris are mapped to points in the image at infinity and is given by $b/r = (1 - \sin^2 i \cos^2 \phi')^{1/2} \psi(\xi, \phi')$. Finally, the Lorentz factor is given by $\gamma = [1 - \beta_{r'}^2(1 - 2/\xi)^{-2} - \beta_{\phi'}^2(1 - 2/\xi)^{-1}]^{-1/2}$.

The emission properties of the debris are described by the local specific intensity, I_{ν_e} . We take the local line profile to be a Gaussian corresponding to a velocity dispersion σ (in units of the speed of light). The width of the local line profile represents not only internal motions of the line-emitting gas (not captured by the SPH simulation) but also the velocity range between the discretized debris points we use in our numerical integration. We further assume that the emissivity of the line is a power-law with radius (see discussion in §4.1 and §5.1). Therefore, we write the specific intensity as

$$I_{\nu_e} = \frac{\epsilon_0 \xi^{-q}}{2(2\pi)^{3/2} \sigma} \exp \left[-\frac{(1 + X - D)^2}{2D^2\sigma^2} \right] \quad (5)$$

where X is defined by $1 + X \equiv \nu/\nu_0$, where ν and ν_0 are observed and rest frame frequency, and ϵ_0 is a constant.

In the final model, the line profiles are described by the following parameters: the inner and outer radius of the line-emitting portion of the debris, ξ_{in} and ξ_{out} , the particle emissivity power-law index q^{tail} and q^{disk} , the inclination of the debris plane i , the local velocity dispersion σ in units of c , and the radius of the central continuum source ξ_0 . The last parameter is relevant to the calculation of the light travel time across the debris, which we describe in §3.2, below.

3.2. Time Delay of the Reprocessed Light Emitted by the Debris

In the emission model we adopt, a central source of finite dimensions illuminates the debris. The luminosity of this source is proportional to the accretion rate onto the black hole. Due to the finite velocity of light, at any given time (in the observer's frame), different portions of the debris are seen to respond to a different level of illumination. It is also noteworthy that the length scales and time scales in this problem span a very large dynamic range. As a consequence, the light-crossing time of the outer portions of the debris is longer than the dynamical time of the inner portions, which makes it necessary for us to follow the re-distribution of the debris in phase space and the variations of the X-ray source carefully.

It is simple to show that travel time delay for light rays can be written as

$$\Delta t_{travel} = (\xi - \xi_0)(1 - \sin i \cos \phi') \quad (6)$$

where ξ and ϕ' are the coordinates of a particle in the orbital plane, ξ_0 is the radius of the central source and i is the inclination. Since light rays travel in the gravitational potential of the black hole they suffer an additional, relativistic time delay, which can be calculated from the

equation of geodesics for photons (Weinberg 1972, p.202). The assumptions are that photons travel in an isotropic gravitational field and that their trajectories can be considered coplanar with the observer and the black hole. We consider only the gravitational delay caused by the black hole's potential and assume that the debris does not have any significant gravitational influence on a light ray. This is a reasonable assumption since $\rho_{debris}/\rho_{bh} \sim 10^{-12}$. In our notation, the gravitational time delay for non-rotating black hole can be expressed as

$$\Delta t_{gr} \cong \left(\frac{\xi - \xi_0}{\xi + \xi_0} \right)^{1/2} + 2 \ln \left[\frac{\xi + (\xi^2 - \xi_0^2)^{1/2}}{\xi \cos i} \right] - \cos \phi' \left[\left(\frac{1 - \cos i}{1 + \cos i} \right)^{1/2} + 2 \ln \left(\frac{1 + \sin i}{\cos i} \right) \right]. \quad (7)$$

The overall delay for a particle caused by light travel and general relativistic effects is then

$$\Delta t = \Delta t_{travel} + \Delta t_{gr}. \quad (8)$$

We only need to account for relative time delays, which we calculate relative to a ray coming from the origin of the coordinate system of the debris. We find that the general relativistic time delay in our calculations never exceeds 10% of the travel time delay, and it is typically of order a few percent.

4. RESULTS AND IMPLICATIONS

4.1. Light Curves and Emissivity of the Debris

The output of the 5k run comprises 351 frames describing the evolution of the debris morphology over 60 days of accretion, with a time step of approximately 4 hours (see Table 1). This is a fine enough temporal resolution to trace the redistribution of particles in the debris. For comparison, a particle at $r = 200 r_g$ orbits the black hole with a period of approximately 24.5 hours. During the accretion phase of the simulation the number of particles decreases due to infall in the black hole. Tracking this number allows us to follow the accretion rate and construct the X-ray light curve. The total amount of mass accreted in this run is about $10^{-2} M_\odot$. The X-rays resulting from accretion illuminate the debris out to large distances from the black hole and power the emission of H α photons.

The output of the 20k run consists of 204 temporal frames spanning 6 days of accretion with a time step of about 45 minutes (the coverage is not even; it includes gaps since the behavior of the debris can be captured even with sparse sampling). Because of the short time span of accretion, the number of accreted particles is small (less than 0.1% of the total mass) and consequently, the illuminating, X-ray light curve is not smooth. To address this issue we compute the H α light curve for two more, fiducial, illumination light curves: one consistent with the debris return rate predicted by theory ($\propto t^{-5/3}$; Rees 1988; Phinney 1989)², and the other, constant in time. This allows us to also examine the effect of different illumination patterns on the line profiles, which we describe in §4.2.

In order to calculate the resulting H α luminosity of the debris it is necessary to determine the efficiency with which

the debris reprocesses the incident radiation. This efficiency can be characterized by the surface emissivity of the debris as a function of radius, $\epsilon = \epsilon_0 \xi^{-q}$, as shown in equation (5). We used the photoionization code CLOUDY (Ferland 1996) for numerical calculations of the response of the debris to illumination. From the calculated surface emissivity as a function of radius ($\text{erg s}^{-1} \text{cm}^{-2}$) we were able to determine the particle emissivity as a function of radius $Q = \epsilon/\Sigma = Q_0 \xi^{-\beta}$ ($\text{erg s}^{-1} \text{particle}^{-1}$), where $\beta = q - p$ is the particle emissivity power-law index, given the surface density distribution of the debris, $\Sigma \propto \xi^{-p}$.

The response generally depends on a spectral energy distribution (SED) of the incident radiation, matter density distribution, and the system geometry. We have described the debris system in terms of these physical parameters and performed CLOUDY calculations.

We have assumed a SED for the illuminating radiation of the form $L_\nu \propto \nu^{-1}$, extending to 100 keV. The normalization for the SED is set by the accretion luminosity of the debris. The mass accreted during the accretion phase of the 5k simulation gives rise to a time-average accretion luminosity of $L_{acc} \approx 1.5 \times 10^{43} M_6 \text{ erg s}^{-1}$, while the maximum luminosity achieved at the beginning of the accretion is $L_{acc}^{max} \approx 8.0 \times 10^{44} M_6 \text{ erg s}^{-1}$ (where $M_6 = M_{bh}/10^6 M_\odot$). The luminosity during flares therefore may exceed the Eddington luminosity, $L_{Edd} = 1.51 \times 10^{44} M_6 \text{ erg s}^{-1}$. For the purpose of CLOUDY calculations, in order to characterize the emissivity of the debris, we have used the time-average value for the accretion luminosity. Our estimated accretion luminosity is comparable to what was observed by Gezari et al. (2003) for three tidal disruption candidates, namely $L_X = 10^{42} - 10^{44} \text{ erg s}^{-1}$.

Based on the particle distribution in the simulation we find that the density in the tidal tail decreases with time because the tail gets stretched as the debris evolves (cf., Figure 1). We find that for the typical SPH time frame the density distribution in the tail can be approximated as $n_H^{tail} \propto \xi$ and is in the range $n_H^{tail} = 10^{14} - 10^{15} \text{ cm}^{-3}$. With path lengths of $9 \times 10^{13} \text{ cm}$ and $\sim 5 \times 10^{15} \text{ cm}$, the corresponding tail column densities are in the range $N_H^{tail} = 10^{27} - 10^{31} \text{ cm}^{-2}$. The low and high values of the column density correspond to lines of sight along the short and long axes of the tail, respectively. (See Table 2 for values of physical parameters in the debris.) The density of particles scattered from the tail in the spheroidal halo around the black hole is fairly low in comparison. The halo density reaches a maximum in the plane of the debris ($\geq 3\sigma$ over-density), where particles orbiting around the black hole form a disk of radius $\sim 2500 r_g$. The number density in the disk decreases with radius as $n_H^{disk} = 1 \times 10^{12} \text{ cm}^{-3} (\xi/500)^{-2.1}$. The corresponding column densities in the directions orthogonally and radially through the disk are $N_H^{disk} \approx 7 \times 10^{20} - 3 \times 10^{25} \text{ cm}^{-2}$, respectively. The spheroidal part of the halo, formed from particles scattered out from the plane of the debris has the estimated number density of $n_H^{halo} = 3 \times 10^{11} \text{ cm}^{-3} (\xi/500)^{-1.4}$ and corresponding column density of $N_H^{halo} \approx 1 \times 10^{25} \text{ cm}^{-2}$.

The CLOUDY calculations show that the H α power emitted by the mostly neutral tidal tail in response to X-

² We have verified that the energy distribution of the debris particles in our simulation would lead to a $\propto t^{-5/3}$ return rate of particles to the pericenter, based on the Keplerian orbits

ray illumination decays with distance from the center as $\epsilon^{tail} \propto r^{-1.6}$, as a consequence of the density distribution in the tail and the geometry of the debris (i.e. illumination incidence). The corresponding particle emissivity for the tail derived from the surface emissivity decays with the distance as $Q^{tail} \propto r^{-2.4}$ (Fig. 3). The disk and the halo components are almost completely ionized and only 1 in 10^7 hydrogen atoms is neutral, on average. The emissivity of the disk decreases with distance from the black hole as $\epsilon^{disk} \propto r^{-2.2}$, approximately. The equivalent particle emissivity distribution for the disk is $Q^{disk} \propto r^{-0.06}$. Therefore, in our description of the surface emissivity of the debris (equation 5) we use power-law indices of $q^{tail} = 1.6$ for the tail and $q^{disk} = 2.2$ for the disk. In our calculation for line profiles and light curves, due to the discrete nature of the SPH simulation, we use the prescription for the emissivity per particle, with power-law indices of $\beta^{tail} = 2.4$ for the tail and $\beta^{disk} = 0.06$ for the disk. The results of the CLOUDY calculations and the power-law prescriptions derived from them are summarized in Figure 3. The total $H\alpha$ luminosities contributed by the tail and the halo for the time-average value of the illumination $L_{acc} = 1.5 \times 10^{43}$ erg s $^{-1}$, as calculated by CLOUDY, are $L_{H\alpha}^{tail} \simeq 1 \times 10^{36}$ erg s $^{-1}$ and $L_{H\alpha}^{disk} \simeq 1 \times 10^{37}$ erg s $^{-1}$. The calculated value of the luminosity for the spheroidal component is $L_{H\alpha}^{halo} \simeq 6 \times 10^{38}$ erg s $^{-1}$ (also listed in Table 2).

We discuss the emission properties of the debris in §5.1 and their implications for the observability in §5.3. Finally, with the above emissivity prescriptions we calculate the *observed* $H\alpha$ luminosity curve of the debris at a particular time step by computing the time at which the light was emitted from the debris and by finding the ionizing flux that was illuminating that location at the time the emission occurred, according to the light-travel time from the black hole to that particular region of the debris.

Figure 4 shows three different $H\alpha$ light curves from the debris confined to a plane (assuming $\xi_{in} = 500$, $\xi_{out} = 40,000$) during the 60-day accretion phase of the 5k simulation. Figure 4a shows the accretion luminosity on a logarithmic scale (solid curve), calculated from the accretion rate of the debris in the SPH simulation. The UV/X-ray luminosity curve is arbitrarily scaled and overplotted on the top of the $H\alpha$ curve for comparison. It is noticeable that the $H\alpha$ light curve departs from the accretion light curve at late times, though the departure appears small in the logarithmic plot (used here due to the large dynamic range of the light curves). The same effect is more noticeable in the Figure 4b, where the accretion luminosity is proportional to $t^{-5/3}$ and the $H\alpha$ light curve is plotted on a linear scale. The $H\alpha$ light curve roughly follows the shape of the incident UV/X-ray light curve at early times but decays faster at late times. The faster decay in the $H\alpha$ light curve reflects the debris evolution in time: as the tail becomes more elongated, the incident photons travel a longer way to illuminate the debris. Consequently, the intensity of the illuminating light gets lower in the later stages of the tidal disruption event. The relative decay rate of the $H\alpha$ light curve with respect to the UV/X-ray light curve diminishes about 80 days after the accretion started. We find that this late relative rise in the $H\alpha$ luminosity is due to the increase of number of particles in the disk component. As particles diffuse from the

high density tail to the lower density disk, in later stages of the simulation, their emission efficiency increases and they contribute a significant amount of $H\alpha$ light to the light curve. To isolate the effect of the debris evolution in time from the evolution of the illuminating light curve, we calculate the $H\alpha$ light curve in the case of constant illumination (Fig. 4c). Here, the relative departure of the $H\alpha$ light curve from the UV/X-ray light curve can be interpreted as a consequence of the expansion and redistribution of the debris. The $H\alpha$ luminosity appears to level off at late times because the debris disk begins to settle into a quasi-steady configuration.

In summary, the *observed* $H\alpha$ flux depends sensitively on the UV/X-ray light curve, on the distribution of matter that makes up the inner portion of the debris, and on how quickly particles redistribute themselves in phase space. The main features of the $H\alpha$ light curve are: an initial rise followed by a decline, with superposed fluctuations. The initial rise is a consequence of the propagation of the initial illumination front through the debris at the speed of light. The fluctuations are a result of the fluctuations in the accretion rate, which are caused, in turn, by the finite number of particles employed in the simulation. The decay rate of the $H\alpha$ light curve is determined by the decay rate of the UV/X-ray light curve, debris expansion and redistribution rate.

4.2. Line Profiles From the Debris and Their Variability

We have computed sample line profiles emerging from the debris for the following choices of model parameters:

1. *Inclination angle of the plane of the debris, i .* – We assumed that the observer is located on the positive z-axis, at a distance $d \rightarrow \infty$ at $i = 30^\circ$ to the z'-axis. Changing the inclination, changes the values of the projected velocities (i.e., the overall width of the line profile) but has very little effect on its shape otherwise.
2. *Inner and outer radius, ξ_{in} and ξ_{out} .* – The adopted inner radius of the debris is the inner boundary of the region from which $H\alpha$ emission is expected to emerge. The choice of the inner radius depends on physical conditions in the debris, as we explain in §5.1. Here, we explore several cases with ξ_{in} between 200 and 10,000. The outer radius $\xi_{out} = 40,000$ is naturally set by the dimensions of the system.
3. *Particle emissivity power-law index, β .* – As noted in §4.1, above, we find that $\beta^{tail} = 2.4$ in the debris tail and $\beta^{disk} = 0.06$ in the disk. These indices describe the emissivity per particle as a power-law and correspond to indices q^{tail} and q^{disk} in the description of the surface emissivity. The adopted values for emissivity indices significantly influence the profile shapes. Higher values of β weigh the emissivity towards smaller radii where the projected velocity is higher.
4. *Velocity dispersion, σ , and central source radius ξ_0 .* – The adopted value of the velocity dispersion for the profiles presented was $\sigma = 100$ km s $^{-1}$. A lower

limit on the velocity dispersion is set by the velocity difference measured for pairs of adjacent particles. This value represents the dispersion due to the finite number of resolving elements in the simulation and equals 20 km s^{-1} for 90% of particles close to the debris plane. The constraint on the upper limit of the velocity dispersion comes from the velocity dispersion due to small scale turbulence, $\sigma_{\text{turb}} \leq (1/2)(L/r)V_{\text{Kepler}} \approx 800 \text{ km s}^{-1}$, where V_{Kepler} is a local circular velocity, r is a distance from the massive black hole and L is the smallest dimension of the fluid (i.e. width or thickness of the tail). Since the real turbulence could be substantially smaller than the upper limit due to dissipation by internal shocks, we adopt a value of 100 km s^{-1} . Larger values of σ produce wider profiles and smooth-out sharp features. The central source radius is arbitrarily chosen to be $\xi_0 = 200$. It implies a central source of finite dimensions such as a corona of ionized plasma, or a vertically extended accretion flow in the innermost parts of an accretion disk. Its effect on the line profiles is rather small.

In Figures 5–9 we show sample line profiles to illustrate how they evolve in time and how they are affected by the choice of model parameters and by the orientation of the observer. Figure 5 is a “trailed spectrogram” summarizing the temporal evolution of the line profiles from the two different SPH runs; it is a 2-dimensional map of the H α emission as a function of projected velocity and time. Figure 6 shows a different representation of the evolution of the line profile with time, which effectively comprises selected time slices from the trailed spectrogram. Figures 7 and 8 show how the inner radius of the line-emitting region and the azimuthal orientation of the observer affect the observed line profiles. Figure 9 shows the effect of the different values of velocity dispersion on the shape of the line profiles. The main properties and features of our results are as follows:

Profile variability with time. – A property that is immediately obvious in the line sequence is the change of the profile shape with time (Figures 5 and 6). It is noticeable that the adopted low value of velocity dispersion allows us to resolve individual particles in the trailed spectrograms, orbiting around the black hole. The evolution of the line intensities in time roughly follows the behavior of the UV/X-ray luminosity but decays somewhat faster in time (see §4.1). The multi-peaked line profile is a consequence of the velocity field of the inner debris, which consists of the inner portion of the tidal tail that is falling towards the black hole (towards the observer) and debris that is rotating around the black hole after being scattered. The line profiles and their variability could be observationally important features of the debris just formed from tidal disruption. The variable line profiles might be observed and recognized on the relatively short time scale of hours to days.

Effect of the inner radius, ξ_{in} . – The profiles become broader as the inner radius of the line-emitting re-

gions decreases since higher-velocity gas resides at smaller radii (see Figure 7). The approximate full width at zero intensity of the profiles ranges from $4,500 \text{ km s}^{-1}$ for $\xi_{\text{in}} = 10,000$ to $18,000 \text{ km s}^{-1}$ for $\xi_{\text{in}} = 200$. We find that line profiles change from the profiles dominated by the emission red-ward from the rest wavelength for $\xi_{\text{in}} < 1000$ to narrower profiles dominated by the blue-ward emission from the tail for $\xi_{\text{in}} > 1000$, since for large values of ξ_{in} , the high-velocity rotating gas in the vicinity of the black hole is excluded and the dominant contributions to the line profile come from the tidal tail. The intensity of the line also decreases with increasing inner radius, making the outer regions of the debris harder to observe.

Effect of observer orientation, ϕ_0 . – Because of the non-axisymmetric geometry and velocity field, the line profiles emitted by the debris, depend on the orientation of the tidal tail relative to the observer. In Figure 8 we show the effect of azimuthal orientation ϕ_0 of the debris, with respect to the observer. The values of ϕ_0 are $45^\circ, 90^\circ, 120^\circ, 180^\circ, 220^\circ$ and 270° , as measured in a counterclockwise direction from positive x' -axis to the observer’s line of sight. These can be compared with the profile corresponding to the same time in Figure 6 for $\phi_0 = 0^\circ$. The position of the peaks in Figure 8 varies relative to the rest wavelength, since the relative direction of bulk motion of the material depends on the observer’s orientation. For example, it is possible to distinguish the emission from the tail for the range of azimuthal orientations $90^\circ - 220^\circ$. The tail emission in these profiles appears as the most blueshifted peak, since these are the orientations for which different portions of the tail flow towards the observer.

Effect of velocity dispersion, σ . – In Figure 9 we show the effect of four different values of the velocity dispersion in calculation of the emission line profiles. A value of 20 km s^{-1} is the lower limit of velocity dispersion set by the discrete nature of the SPH simulation, while the upper limit of 800 km s^{-1} is determined by the small scale turbulence in the debris. The velocity dispersion of particles in the halo (about 1500 particles in the 20k run) is significantly higher and reaches 6000 km s^{-1} . As the value of the velocity dispersion increases the profile features get smoothed out, until only a smooth, double-peaked profile is observed.

Effect of illuminating light curve. – We have computed model profiles for several different X-ray illumination light curves keeping all the other parameters fixed. We used (a) the light curve obtained from the accretion rate in the 5k simulation, (b) the light curve from the accretion rate as predicted by theory, i.e. $\propto t^{-5/3}$ (Rees 1988; Phinney 1989), and (c) a light curve that is constant in time (Figure 4). We find that the line profile shapes do not depend sensitively on the shape of the light curve. This is a consequence of the centrally “weighted” emissivity profile of the debris which causes the innermost

emission region to be the dominant contributor of the $H\alpha$ light. In the innermost region of the debris the dynamic range in light-travel times is not large; therefore the illumination of the innermost emitting region is almost instantaneous. Over the very short light-crossing time of the central emitting region, the gradient in the UV/X-ray light curve is small and the illumination is nearly constant over this region. The fast fluctuations in the illuminating light curve on the other hand are smoothed out during reprocessing in the debris, and cannot be identified in the $H\alpha$ light curve.

In summary, we find that profiles are not significantly influenced by the shape of the illuminating light curve. The profile shapes are affected, however, by the inner radius of the line-emitting region and redistribution of the debris. The inner radius can change with the advance or recession of the ionization front into the debris, which is controlled primarily by the density of the debris. The most notable effect of the inner radius is on the width of the profile. Since the physical conditions can change very rapidly during flares, this mechanism causes the line profiles to change on the light crossing time scale (minutes to hours) and evolve from wide multi-peaked to narrow and vice versa (the recombination time is negligible in comparison to the light-crossing time of the debris, therefore particles in the debris respond effectively instantaneously to changes in the incident flux). The redistribution of the debris in phase space, on the other hand takes more time: ~ 24 hours for particles in the innermost part of the emitting region. This redistribution of the debris also may cause a transition from narrower to wider profiles, however it takes place gradually, on the time scale of days.

5. DISCUSSION

5.1. *Physical Conditions in the Debris and Radiative Processes*

We have calculated the physical conditions and radiative processes in the debris using the photoionization code CLOUDY, version 94 (Ferland 1996). It is necessary to know the physical conditions in order to assess the validity of the assumptions made in our line profile calculations.

Since the physical conditions in the tidal tail, disk and halo differ noticeably, these three regions naturally emerge as separate components of the tidal debris. The spheroidal halo is an oblate structure of particles scattered out of the plane of the debris. The disk is produced by the flow of particles from the tail which turn around the black hole and form a higher density circular component concentrated close to the plane of the debris. The disk shows a smooth transition to the halo in terms of density and physical parameters (see Table 2). The physical differences among the components arise as a consequence of the number density, which is several orders of magnitude higher in the tail. The particle density of the halo is uncertain, due to the numerical scatter, and consequently its luminosity contribution is also subject to uncertainty. We nevertheless have calculated and presented physical properties of the spheroidal component, as given by the SPH simulation, and we discuss the implications of its presence for the line profiles and the observability in the next section.

The temperature of the debris tail reaches 3×10^4 K in the hottest parts of the tail (i.e. the illuminated face of the tail) and equals 5000 K on average in the partially ionized and neutral parts of the tail. The temperature in the disk ranges from 8000 K in the inner region to 1×10^6 K at the outer rim of the disk, with the average $\sim 10^5$ K. The mean temperature of the halo is 1×10^4 K and ranges from 3×10^7 K in the central parts of halo, to 1×10^4 K in the outer halo. The ionization parameter is calculated for all components as $U \equiv \Phi_H / n_H c$, where Φ_H is the flux of ionizing photons, n_H is the total hydrogen density, and c is the speed of light. The ionization parameter in the tail ranges from 0.1 in the parts of the tail closest to the source of ionization, to 10^{-5} on the far side of the tail. The ionization parameter in the disk is almost constant throughout the disk with a value of about 20. The ionization parameter in the halo is higher with an average value of about 27. As a consequence, the disk and the halo are in a much higher state of ionization relative to the tail. The disk shows a wide range of hydrogen ionization fractions over its radius, with the strongest ionization at the outer rim of the disk where density is lowest. In the halo the fraction of neutral hydrogen atoms ranges from 10^{-10} to 10^{-7} , with an average value close to 10^{-7} . In contrast, the tail is mostly neutral, with only one hydrogen ion per 10^3 hydrogen nuclei. The properties of the tidal disruption regions are summarized in Table 2.

The ionization state of the debris as well as its abundance and density determine the radiative processes dominant in the debris. The implication of the assumed solar metallicity is that emission lines from metals play an important role in the cooling of the debris. We focus our attention on processes relevant to the final $H\alpha$ luminosity. Two processes contribute to the $H\alpha$ luminosity of the debris: recombination and collisional excitation. The dominant recombination channel is the recombination of a photoelectron to the $n = 3$ level followed by a decay to the $n = 2$ level via emission of an $H\alpha$ photon. Emission by collisional excitation occurs when hydrogen atoms in the $n = 1$ and $n = 2$ levels are promoted to the $n = 3$ level by collisions with energetic photoelectrons and then de-excite radiatively. The relative contribution of $H\alpha$ emission through recombination relative to collisions is

$$\frac{L_{H\alpha,rec}}{L_{H\alpha,coll}} = \frac{\alpha_{rec} n_{HII} V_{rec}}{\alpha_{coll} n_{HI} V_{coll}} \quad (9)$$

where α_{rec} and α_{coll} are the respective coefficients for recombination and collision processes which lead to emission of an $H\alpha$ photon, n_{HII} and n_{HI} are the number density of hydrogen ions and atoms, and V_{rec} and V_{coll} are the parts of the debris volume which gives rise to emission through recombination and collisional de-excitation, respectively.

The recombination coefficient for an electron to recombine from the continuum to the $n=3$ level can be written as $\alpha_C = \sum_{n=3}^{\infty} \alpha_n$ for a given temperature. The adopted recombination coefficients for the tail and halo are $\alpha_{rec}^{tail} = 3.4 \times 10^{-13} \text{ cm}^3 \text{ s}^{-1}$, $\alpha_{rec}^{disk} \simeq 1.8 \times 10^{-14} \text{ cm}^3 \text{ s}^{-1}$, and $\alpha_{rec}^{halo} = 1.8 \times 10^{-13} \text{ cm}^3 \text{ s}^{-1}$ (Osterbrock 1989). Similarly, it is possible to estimate the rate of collisions which will promote an electron to $n=3$ state. The high optical depths in the Lyman series cause a significant electron population in the $n = 2$ level. The photoelectron

energy distribution for low-energy levels of hydrogen differs from the Boltzmann distribution and the number density is not sufficiently high for collisions to lead to thermal equilibrium (Eq. 10.57 of Krolik 1999). In particular, thermalized energy levels will be $n > 1$ for the tail, $n > 2$ for the halo, and $n > 3$ for the disk, and the relative populations of these levels will be in agreement with their statistical weights. It is possible then to estimate the collisional excitation coefficients for transitions from the $n=1$ and $n=2$ levels to the thermalized $n=3$ level (Eq. 3.21 of Osterbrock 1989). This approximately yields collisional excitation rates for the tail, disk and halo of $\alpha_{coll}^{tail} = 1.2 \times 10^{-11} \text{ cm}^3 \text{ s}^{-1}$, $\alpha_{coll}^{disk} = 1.1 \times 10^{-9} \text{ cm}^3 \text{ s}^{-1}$, and $\alpha_{coll}^{halo} = 9.0 \times 10^{-11} \text{ cm}^3 \text{ s}^{-1}$.

With the values of the rate coefficients, the ionization state of the tail, disk and halo ($n_{HII}/n_H \approx 10^{-3}$ in the tail and 10^7 in the halo and disk on average), and taking into account the ratio of emitting volumes for two processes, it is possible to calculate the ratio of respective relative contributions from recombination and collisions from equation (9) to be about 1×10^{-6} , 6×10^3 , and 2×10^4 . These values are not unexpected: collisional excitation is the dominant mechanism for production of $H\alpha$ photons in the tail, where the density is highest, while recombination is dominant in the disk and halo.

Some of the $H\alpha$ photons created by the two processes are destroyed on the way out of the debris. The mechanisms that impact the total output in $H\alpha$ luminosity are the absorption in the $H\alpha$ transition, and electron scattering, with respective optical depths $\tau_{H\alpha}$ and τ_e . The optical depth $\tau_{H\alpha}^{tail}$ is very high for the $H\alpha$ photons traveling across the tail, along the lines of incidence of illuminating photons and typically has a value of order 10^7 . Electron scattering in the tail has an average optical depth of $\tau_e^{tail} \approx 10$. Consequently, the majority of $H\alpha$ photons are created in the thin ionized and partially ionized layers of the tail (we refer to them as the tail “skin”). From here a certain fraction of $H\alpha$ photons escapes the debris and reaches the observer. In the disk $\tau_{H\alpha}^{disk} \approx 4 \times 10^6$ and $\tau_e^{disk} \approx 8$. In the early stages of accretion, while the luminosity is still super-Eddington, the halo is optically thin to $H\alpha$ photons ($\tau_{H\alpha}^{halo} \approx 2 \times 10^{-2}$) and the electron scattering optical depth is about $\tau_e^{halo} \approx 5$. In the late stages of the debris evolution $\tau_{H\alpha}^{halo} \approx 1 \times 10^4$ and τ_e stays approximately the same in the halo. The high values of τ of the halo material destroy the fraction of the $H\alpha$ photons emitted by the part of the debris embedded in the halo. The evolution of the spherical halo would further help the process of fading of $H\alpha$ emission with time along with the decreasing accretion luminosity. For the purposes of radiative transfer calculations we have modeled the tail, the disk and the halo as three *separate* components and therefore we do not account for the secondary absorption and electron scattering by the halo, of $H\alpha$ photons created in the tail. Both opacity mechanisms cause the destruction of $H\alpha$ photons, if the spherical halo is fully evolved, and possibly wipe out the $H\alpha$ emission line. If the same process operates in the centers of galaxies which are tidal disruption candidates, it should be possible to observe the disappearance of the broad $H\alpha$ emission line on the scale of months.

5.2. Spheroidal Halo: Implications for Line Profiles and Luminosity

In our predictions of the observational signature of the post-disruption debris we have not included any contributions from the spheroidal halo because we doubt that this structure, as predicted by our SPH simulation is real. In this section we discuss this issue further and justify our approach. We also describe qualitatively the effect of such a halo on the observational appearance of the debris.

The halo is very likely produced artificially because a number of particles is scattered from the disk every time the flow of particles turns around the black hole and intersects with the inflowing stream of particles. The number of particles contributed to the halo by numerical scatter is proportional to \sqrt{N} , where N the total number of particles in the run, and multiplied by a factor τ_{run}/τ_{dyn} , as described in §2. The dynamical time scale of the disk is about 7 days for the outermost particles, which implies that the number of scattered particles is of the order of 1000. This is an upper limit of the uncertainty, where total number of particles in the halo, in the 20k run, reaches number of 1500 particles in the later stages of the debris evolution.

It has been pointed out by several authors that a spheroidal halo (Ulmer, Paczynski & Goodman 1998; Loeb & Ulmer 1997; Cannizzo et al. 1990; Alexander & Livio 2001) with a central radiatively supported torus (Rees 1988; Loeb & Ulmer 1997; Cannizzo et al. 1990; Evans & Kochanek 1989) may form around the black hole as a consequence of a self-compression of the flow, which leads to the ejection of the debris with high velocities, perpendicular to the plane. However, none of the above mentioned structures were resolved beyond doubt in the simulations. A halo-like structure is expected to be in hydrostatic equilibrium, and its size should be determined by the radiation pressure from the central source. Ulmer, Paczynski & Goodman (1998) and Loeb & Ulmer (1997) argue that the luminosity incident upon the halo can rarely be exactly tuned for the structure to rest in equilibrium. They further calculate that for a super-Eddington luminosity the halo will expand and cool down on the time scale of months to years, until it becomes gravitationally unbound and is blown away. For a sub-Eddington luminosity, on the other hand, the halo is expected to collapse due to insufficient support from radiation pressure.

Based on its physical conditions it is obvious that, if real, the halo observed in our simulations would make the dominant contribution to the line emission from the debris. In the late stages of the debris evolution, our simulations show the halo becoming optically thick to $H\alpha$ photons. Moreover, the long diffusion time of photons in the halo ($t_{diff} \sim \tau_e r/c \approx 3.5$ hours, where r the is inner radius of the halo) may smear out the time variability of the emission line profiles, which is one of the main signatures of the disruption event. The high value of the velocity dispersion of the particles in the halo would smear out the line profiles and very likely make them unobservable. It is therefore necessary to address in future studies what fraction of the halo (if any) is really present and what fraction is contributed by the numerical scatter.

If a halo manages to form, survives the super-Eddington phase, and achieves hydrostatic equilibrium it will be

transparent to $H\alpha$ photons only during the super-Eddington phase. At later times, we expect that it will become optically thick and will be the primary source of illumination of the outer debris. Moreover, it will fade on a time scale of months to years. In this picture, which is consistent with the predictions of Loeb & Ulmer (1997), the shape of the observed line profiles should be similar to the profiles computed here for large values of the inner radius (see Figure 7). Whether the profile (noticeable here for $\xi = 10,000$ at the wavelength $\lambda = 6500\text{\AA}$) will appear as blueshifted or redshifted would depend on the orientation of the debris tail with respect to the observer.

5.3. Observability of Emission Lines and Their Uniqueness as a Tidal Disruption Signature

The CLOUDY calculation predicts a time-average $H\alpha$ luminosity from the tidal debris of about 10^{36} , 10^{37} , and 6×10^{38} erg s^{-1} for the tail, disk and halo, respectively. In the earlier stages of the disruption event when the UV/X-ray luminosity is super-Eddington, the $H\alpha$ luminosity is expected to be up to 80 times higher than its average value and comparable to that of tidal disruption candidates observed in the local universe (see Figure 4). The examples are NGC 4450 (at 16.8 Mpc) with an $H\alpha$ luminosity of $L_{H\alpha} = 1.8 \times 10^{39}$ erg s^{-1} (Ho et al. 2000) and NGC 1097 (at 22 Mpc) with $L_{H\alpha} = 7.7 \times 10^{39}$ erg s^{-1} (Storchi-Bergmann et al. 1995). Thus the emission-line signature of a tidal disruption event should be detectable at least out to the distance of the Virgo cluster. In practice, however, the detection of such emission lines from low luminosity sources may be complicated by the weak contrast relative to the underlying stellar continuum.

Based on observational constraints from known tidal disruption candidates, it should be possible to detect some variable properties of the line profiles and light curves predicted here. One of the first observable effects of tidal disruption should be UV/X-ray flash accompanied by a decaying light curve, mirrored in the delayed response of the $H\alpha$ light curve of the debris, with some scatter. The line profile intensities are expected to decay accordingly in time. Other effects to look for are the change in the number of peaks in the line profile, relative fluctuations in intensity of the peaks as well as their shift in wavelength.

The temporal variability of the $H\alpha$ emission line profiles from the post-disruption debris is one of the important indicators of a tidal disruption event. In order to capture the rapid profile variability, due to the variable illumination, the exposure time should be comparable to the light crossing time of the innermost regions of the line-emitting debris, which has the fastest and strongest response to the ionizing radiation. Longer exposures are expected to capture the average shape of the rapidly varying line profiles. The light-crossing time of the innermost regions of the debris is about $8 \xi_2 M_6$ minutes (where $\xi_2 = \xi/100$), while the exposure times are typically about 30-60 minutes (for galaxies at the distance of the Virgo cluster, for example). Thus, if an event is caught early in its evolution and the light-crossing time is relatively long (i.e., $M \gtrsim 10^6 M_\odot$), there is a chance of detecting variability caused by changing illumination over the course of one to a few nights. On longer time scales, variability is caused by changes in the structure of the debris. In the presence of the spheroidal

halo, the variability of the lines may be modified by the long diffusion time scale of photons through the halo. The component of the tidal tail outside the halo will then still respond to the variability but on the time scale set by the light reprocessed by the halo.

In view of the predictions from our profile calculation, an important question is whether variable multi-peaked line profiles can originate in some other physical scenario or can be regarded as the unique signature of tidal disruption. Multi-peaked emission lines are likely to be the signature of an inhomogeneity in the phase-space distribution of the emitting material. Due to the asymmetry of the emitting region, the direction of the observer has a large influence on the observed line profile, making it difficult, if not impossible, to infer the exact emission geometry from a particular multi-peaked profile. Nevertheless the variability pattern of the line profiles can serve as a general indicator of a tidal disruption event. Additional observational indicators can be used in conjunction to diagnose a tidal disruption event, for example, a sharp X-ray/UV flash preceding the appearance of the emission lines, an emission line spectrum indicative of a hard ionizing continuum (i.e., the presence of ionic species with high ionization potentials), and the characteristic decay of the emission-line flux on time scales of weeks to months after the event (the flux of different emission lines is expected to decay at different rates; see, for example, Eracleous, Livio, & Binette 1995).

5.4. Approximations in the Calculation

The finite resolution of the simulation could introduce uncertainties in the accretion light curve caused by the discretized accretion of the stellar material onto the black hole. Another possible effect is that the finite number of particles does not completely reveal the morphology of the debris and some of its components may stay hidden. For example, when the majority of the particles are confined to the tail it is hard to say if there is an accretion disk forming around the black hole out of a small number of particles. Consequentially, there is a concern that profiles calculated for low values of the inner radius, i.e. $\xi_{in}=200$, may represent the contribution from a small number of particles in the central region and therefore dominated by small-number noise.

A possible source of error is the assumption of a *thin, flat* structure (i.e., confined to a plane). In the early stages of the evolution of the debris, the majority of the particles are still in the tidal tail, located in a plane, which makes the assumption valid. During the evolution of the debris the number of particles that orbit around the black hole in an almost spherical distribution increases (Cannizzo et al. 1990; Loeb & Ulmer 1997; Ulmer, Paczynski & Goodman 1998; Ulmer 1999; Menou & Quataert 2001). At that point it is possible to distinguish three structural components of the debris: the relatively planar tidal tail and the disk and the spheroidal halo. The halo is made up of particles scattered from the tail by shocks during the pericentric approach of the debris or during the intersection of the tail with itself (Kochanek 1994; Lee, Kang, & Ryu 1996; Kim et al. 1999; Ayal et al. 2000) and some fraction of particles contributed by the numerical noise. Since the tidal tail includes the majority of the particles, and most

of the halo mass is concentrated close to the equatorial plane, even in our last frame, the assumption of a thin disk is still reasonable. If, however, the mass in the spherical halo increases at very late times, the assumption of a planar geometry needs to be reconsidered.

We also adopt the weak field approximation in our calculations, which is a fairly small source of error (of order 1% and less). This is valid since we adopt $\xi_{in} = 100$ as the innermost radius of the line-emitting debris. The few particles interior to this radius would not contribute to the H α emission because their close proximity to the source of ionizing radiation would make them fully ionized. In the case of a physical scenario where emission of H α is not possible because of a highly ionized debris, the same profile formalism can be used to calculate the emission from other lines emitted under these conditions.

6. CONCLUSIONS

We modeled the emission-line luminosity and profile from the debris released by the tidal disruption of a star by a black hole in the early phase of evolution. Our model predicts prompt optical evolution of post-disruption debris and profile shapes different from circular and elliptical disk model profiles. Since line profiles observed so far in LINERS look more disk-like and evolve slowly, the observations are likely to have caught the event at late times (≥ 6 months after the initial disruption), after the debris has settled into a quasi-stable configuration.

The line profiles can take a variety of shapes for different orientations of the debris tail relative to the observer. Due to the very diverse morphology of the debris, it is almost impossible to uniquely match the multi-peaked profile with the exact emission geometry. Nevertheless, the profile widths and shifts are strongly indicative of the velocity distribution and the location of matter emitting the bulk of the H α light. Profile shapes do not depend sensitively on the shape of the light curve of the X-rays illuminating the debris. They strongly depend on the distance of the emitting material from the central ionizing source, which is a consequence of the finite propagation time of the ionization front and the redistribution of the debris in phase space. It may be possible to distinguish

between the two effects observationally, based on their different characteristic time scales. The onset of the optically thick spheroidal halo should cause the disappearance of the broad H α emission line on the time scale of months, and give rise to the emission of narrower, strong, blueshifted or redshifted emission line, arising from the portion of the tidal tail unobscured by the halo.

If X-ray flares and the predicted variable profiles could be observed from the same object they could be used to identify the tidal disruption event in its early phase. The X-ray flares can be promptly detected by all-sky synoptic X-ray surveys and high energy burst alert missions such as *Swift*. The evolution of the tidal event may then be followed with optical telescopes from the ground on longer time scales and give an insight in the next stage of development of the debris. Thus, simulations of the tidal disruption process on longer time scales (of order several months to a few years) are sorely needed. Calculations of the long-term evolution of a tidal disruption event can predict the type of structure that the debris finally settles into and whether its emission-line signature resembles the transient double-peaked lines observed in LINERS. This study would provide an important insight into the evolution of LINERS.

Finally, the observed rate of tidally disrupted solar type stars can constrain the rate of captured compact objects (which are important gravitational wave sources), and the capture rate of main sequence stars in our Galaxy, which are expected to emit the peak of the gravitational radiation in the LISA frequency band and can be detected in the local universe.

We are indebted to J. Charlton for her help with CLOUDY. T.B. also thanks M. Falanga for his valuable comments. We are also grateful to the anonymous referee for very insightful and helpful comments and suggestions. We acknowledge the support of the Center for Gravitational Wave Physics funded by the NSF under cooperative agreement PHY-0114375, NSF grants PHY-9800973 and PHY-0244788, the Zaccheus Daniel Fellowship, and the Eberly College of Science.

REFERENCES

- Alexander, T. & Kumar, P. 2001, ApJ, 549, 948
 Alexander, T. & Livio, M. 2001, ApJ, 560, L143
 Alexander, T. 2003, Carnegie Observatories Astrophysics Series, Vol.1: Coevolution of Black Holes and Galaxies, 2003, ed. L.C.Ho (Pasadena: Carnegie Observatories)
 Alexander, T. & Morris, M. 2003, ApJ, 590, L25
 Alexander, T. & Hopman, C. 2003, ApJ, 590, L29
 Ayal, S., Livio, M., & Piran, T. 2000, ApJ, 545, 772
 Bade, N., Komossa, S., & Dahlem, M. 1996, A&A, 309, L35
 Bicknell, G. V. & Gingold, R. A. 1983, ApJ, 273, 749
 Bower, G.A. 2000, AJ, 111, 5
 Brandt, W. N., Pounds, K., & Fink 1995, MNRAS, 273, L47
 Burderi, L., King, A. R. & Szuszkiewicz, E. 1998, ApJ, 509, 85
 Cannizzo, J. K. Lee, H. M., & Goodman, J. 1990, ApJ, 351, 38
 Cappellari, M. et al. 1999, ApJ, 519, 117
 Carter, B. & Luminet, J. P. 1982, Nature, 296, 211
 Carter, B. & Luminet, J. P. 1983, A&A, 121, 97
 Chen, K., Halpern, J.P. & Filippenko, A.V. 1989, ApJ, 339, 742
 Chen, K., Halpern, J.P. 1989, ApJ, 344, 115
 Collin-Souffrin, S. & Dumont, A.M. 1989, A&A, 213, 29
 David, L. P., Durisen, R. H., & Cohn, H. N. 1987, ApJ, 313, 556
 David, L. P., Durisen, R. H., & Cohn, H. N. 1987, ApJ, 316, 505
 Diener, P. et al. 1997, ApJ, 479, 164
 Di Stefano, R., Greiner, J., Murray, S., & Garcia, M. 2001, ApJ, 551, L37
 Donley, J. et al. 2002, AJ, 124, 1308
 Duncan, M. J. & Shapiro, S. L. 1982, ApJ, 253, 921
 Eckart, A., Ott, T. & Genzel, R. 1999, A&A, 352, L22
 Eracleous, M. & Halpern, J.P. 1994, ApJS, 90, 1
 Eracleous, M. & Halpern, J.P. 2001, ApJ, 554, 240
 Eracleous, M. & Halpern, J.P. 2003, ApJ, 599, 886
 Eracleous, M., Livio, M., & Binette, L. 1995, ApJ, 445, L1
 Eracleous, M., Livio, M., Halpern, J.P. & Storchi-Bergmann, T. 1995, ApJ, 438, 610
 Evans, C. R. & Kochanek, C. S. 1989, ApJ, 346, L13
 Ferland, G. J. 1996, Hazy, a Brief Introduction to CLOUDY (Lexington: Univ. Kentucky, Dept. Phys. Astron.)
 Figer, D. F. et al. 2000, ApJ, 553, L49
 Frank, J. & Rees, M. J. 1976, MNRAS, 176, 633
 Frank, J. 1978, MNRAS, 184, 87
 Freitag, M. 2001, Class. Quant. Grav., 18, 4033
 Freitag, M. & Benz, W. 2002, A&A, 394, 345
 Freitag, M. 2003, ApJL, 583, L21
 Frolov, V. P. et al. 1994, ApJ, 432, 680
 García-Senz, D., Bravo, E., & Woosley, S. E. 1999, A&A, 349, 177
 Gezari, S. et al. 2003, ApJ, preprint
 Gezari, S. et al. 2002, ApJ, 576, 790

- Ghez, A. M. et al. 2000, *Nature*, 407, 349
 Greiner, J. et al. 2000, *A&A*, 362, L25
 Grupe, D. et al. 1995a, *A&A*, 299, L5
 Grupe, D. et al. 1995b, *A&A*, 300, L21
 Grupe, D., Thomas, H.-C., & Leighly, K. M. 1999, *A&A*, 350, L31
 Heckman, T. M., 1980, *A&A*, 87, 152
 Hills, J. G. 1975, *Nature*, 254, 295
 Hills, D & Bender, P. L. 1997, *ApJ*, 445, L7
 Ho, L.C. et al. 2000, *ApJ*, 541, 120
 Ivanov, P. B. & Novikov, I. D. 200 1, *ApJ*, 549, 467
 Ivanov, P. B., Chernyakova, M. A., & Novikov, I. D. 2003, *MNRAS*, 338, 147
 Khokhlov, A., Novikov, I. D., & Pethick, C. J. 1993, *ApJ*, 418, 181
 Kim, S. S., Park, M.-G., & Lee, H. M. 1999, *ApJ*, 519, 647
 Kochanek, C. S. 1994, *ApJ*, 422, 508
 Komossa, S. & Greiner, J. 1999, *A&A* 349, L45
 Krabbe, A. et al. 1991, *ApJ*, 382, L19
 Krolik, J.H. 1999, *Active Galactic Nuclei*, (New jersey: Princeton)
 Laguna, P., Miller, W. A. & Zurek, W. H. 1993a, *ApJ*, 404, 678
 Laguna, P. et al. 1993b, *ApJ*, 410, L83
 Lee, H. M., Kang, H., & Ryu, D. 1996, *ApJ*, 464, 13
 Li, L., Narayan, R., & Menou, K. 2002, *ApJ*, 576, 753
 Lightman, A. P. & Shapiro, S. L. 1977, *ApJ*, 211, 244
 Loeb, A., & Ulmer, A. 1997, *ApJ*, 489, 573
 Magorrian, J. & Tremaine, S. 1999, *MNRAS*, 309, 447
 Marck, J. A., Lioure, A., & Bonazzola, S. 1996, *A&A*, 306, 666
 Menou, K. & Quataert, E. 2001, 562, L140
 Murphy, B. W., Cohn, H. N., & Durisen, R. H. 1991, *ApJ*, 370, 60
 Najarro, F. et al. 1994, *A&A*, 285, 573
 Novikov, I. D., Pethick, C. J., & Polnarev, A. G. 1992, *MNRAS*, 255, 276
 Osterbrock, D.E. 1989, *Astrophysics of gaseous Nebulae and Active Galactic Nuclei* (University Science Books)
 Phinney, E.S. 1989 in *IAU Symp. 136, The Center of the Galaxy*, ed. M.Morris (Dordrecht: Kluwer), 543
 Rees, M. 1988, *Nature*, 231, 91
 Renzini, A. et al. 1995, *Nature*, 378, 39
 Rybicki, G.B. & Lightman, A.P. 1979, *Radiative Processes in Astrophysics* (New York:Wiley)
 Sembay, S. & West, R. G. 1993, *MNRAS*, 262, 141
 Shields, J.C. et al. 2000, *ApJ*, 534, L27
 Schöedl, R. et al. 2002, *Nature*, 419, 694
 Siemiginowska, A., Czerny, B., & Kostyunin, V. 1996, *ApJ*, 458, 491
 Sigurdsson, S. & Rees, M. J. 1997, *MNRAS*, 284, 318
 Storchi-Bergmann, T., Baldwin, J.A. & Wilson, A.S 1993, *ApJ*, 410, L11
 Storchi-Bergmann, T. et al. 1995, *ApJ*, 443, 617
 Storchi-Bergmann, T. et al. 1997, *ApJ*, 489, 87
 Strateva, I. V., et al. 2003, *AJ*, 126, 1720
 Syer, D. & Clarke, C. J. 1992, *MNRAS*, 255, 92
 Syer, D. & Ulmer, A. 1999, *MNRAS*, 306, 35
 Ulmer, A. 1999, *ApJ*, 514, 180
 Ulmer, A., Paczynski, B & Goodman, J. 1998, *A&A*, 333, 379
 Weinberg, S. 1972, *Gravitation and Cosmology: Principles and Applications of the General Theory of Relativity* (New York: Wiley)
 Yu, Q. 2003, *MNRAS*, 339, 189

TABLE 1
PARAMETERS OF SPH RUNS

SPH Run	Total Particles	Total Duration (days)	Start of Accretion (days)	Emission-Line Evolution (days)	Time Step (hours)	Particle Mass (g)
5k	5000	94	34	60	4.11	3.978×10^{29}
20k	20000	53	47	6	0.746	9.945×10^{28}

TABLE 2
PHYSICAL PROPERTIES OF THE DEBRIS

Debris Region	N_H^a (cm ⁻²)	n_H (cm ⁻³)	n_{HI}/n_{Htot}	n_{HII}/n_{Htot}	T^b (K)	U ^c	$L_{H\alpha}^d$ (erg s ⁻¹)
Tail	$10^{27}-10^{31}$	$10^{14}-10^{15}$	~ 1	$\sim 10^{-3}$	5×10^3	$10^{-5}-0.1$	1×10^{36}
Disk	$10^{21}-10^{25}$	$10^{11}-10^{12}$	$10^{-8}-0.3$	0.7-1	$\sim 1 \times 10^5$	20	1×10^{37}
Halo	10^{25}	10^9-10^{12}	$\sim 10^{-7}$	~ 1	1×10^4	27	6×10^{38}

^aThe column density: low and high values correspond to directions orthogonally and radially through the debris component.

^bThe average value of temperature over radius.

^cIonization parameter: range of values in the tail and average in the disk and halo.

^dThe H α luminosities from the debris components as calculated for the time-average value of incident luminosity $L_{acc} = 1.5 \times 10^{43}$ erg s⁻¹.

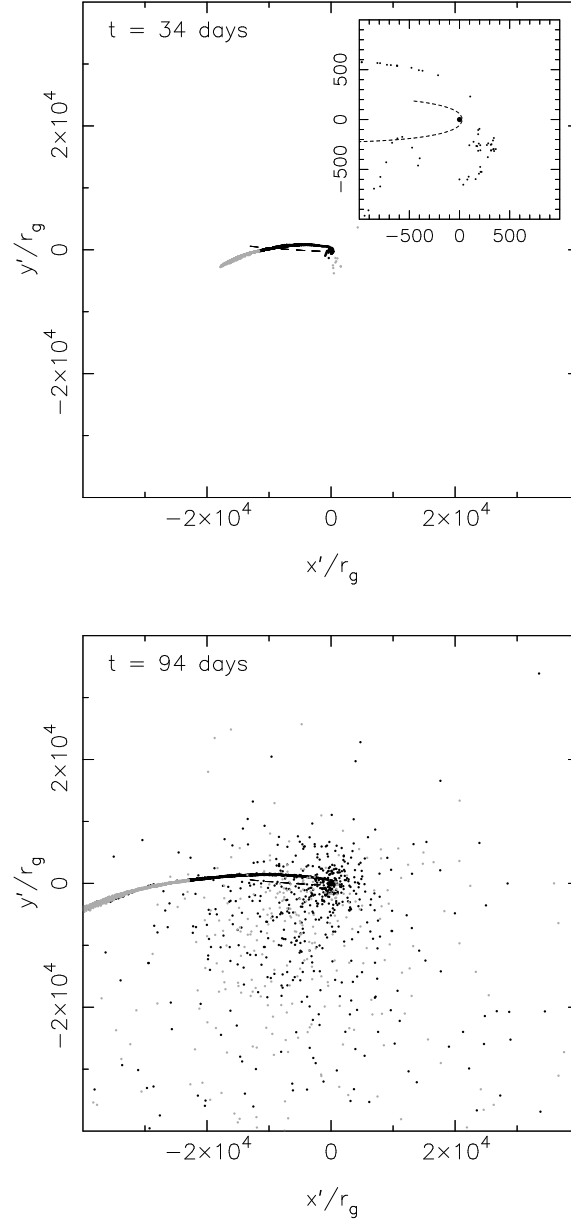


FIG. 1.— Maps showing the positions of the SPH particles from the 5k simulation after the second pericentric passage, projected in the $x'y'$ -plane at two different times. Particles gravitationally bound to the black hole are colored black, while the unbound particles are colored grey. The dashed line represents the initial trajectory of the star before disruption and the trajectory of the center of mass of the debris after disruption. The maximum particle velocities are of order $10^{-2}c$. *Upper Panel:* Particle map at the start of the accretion phase, 34 days after the disruption occurred. Inset: Particles in the inner region of the debris, orbiting close to the black hole. *Lower Panel:* Particle map at the end of the simulation, 94 days after the disruption. The tidal tail can be clearly separated into particles that are unbound and about to escape the black hole and particles that are returning towards the black hole. The inner region of the debris consists of returning particles from the inner tail that have been scattered and form a rotating structure around the black hole.

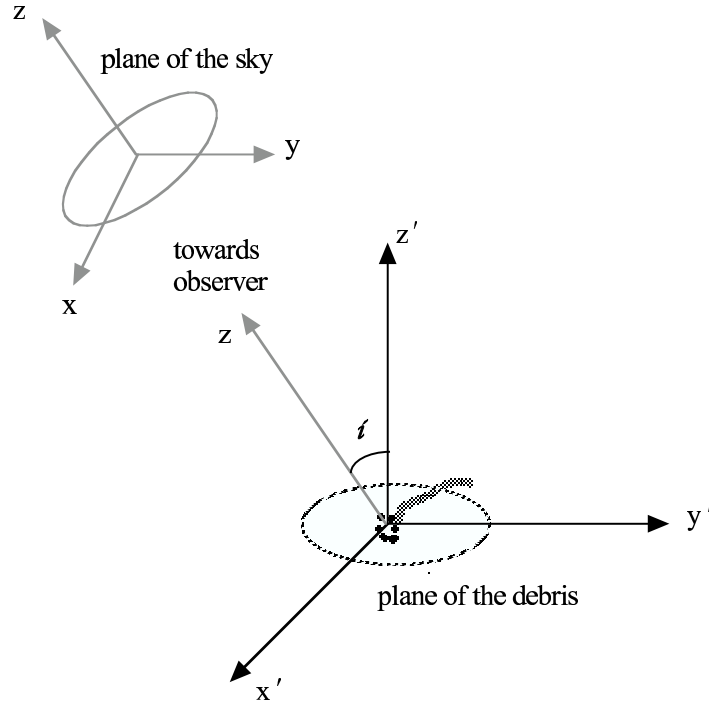


FIG. 2.— The general scheme of the debris geometry used in the profile calculations. The debris field lies within the $x'y'$ -plane, while the observer is located at the infinity in the direction of the z -axis, with a line of sight that makes an angle i to the z' -axis.

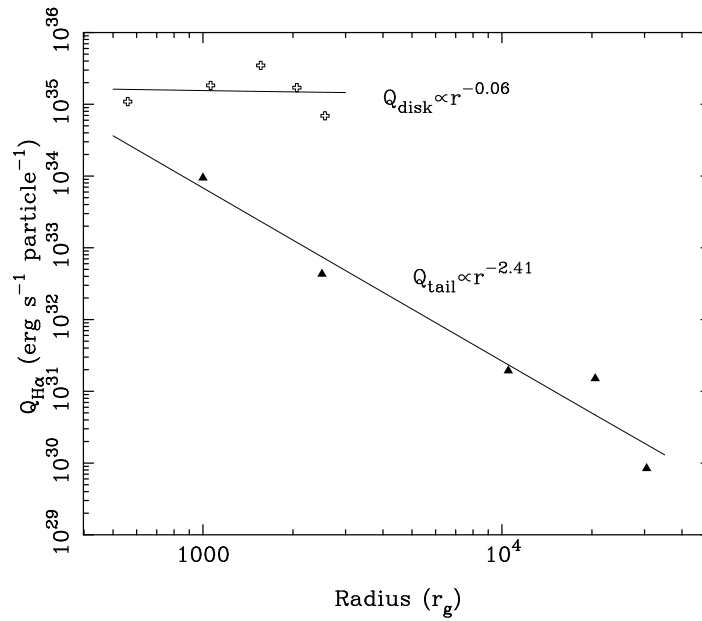


FIG. 3.— The quantum efficiency for particles in the disk (upper) and the tail (lower) as a function of distance from the black hole. The data points are the results of CLOUDY photoionizations calculations performed for different regions in the tail and the disk. The solid line is the best fit power law, with power law index, $q^{\text{tail}}=2.41$ and $q^{\text{disk}}=0.06$, respectively.

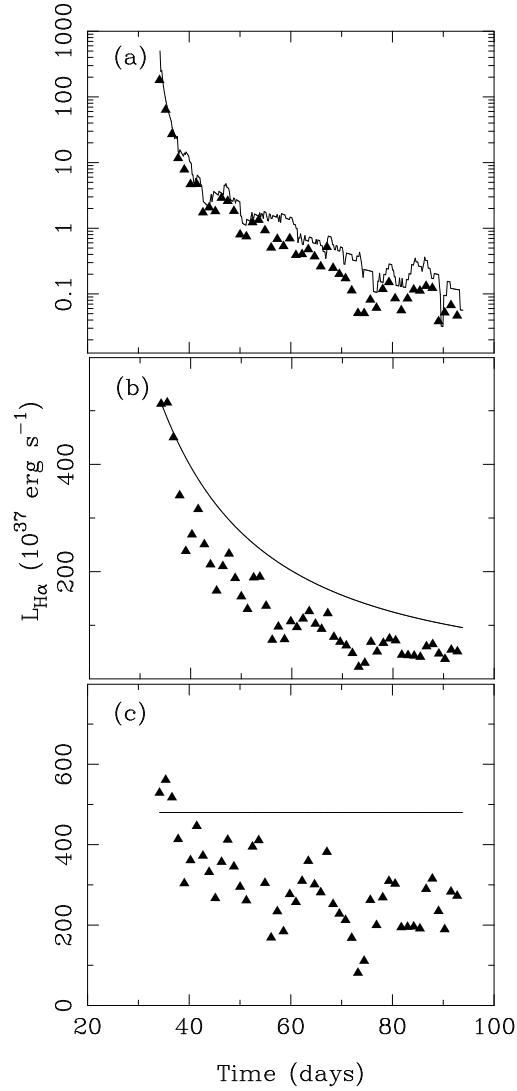


FIG. 4.— The $\text{H}\alpha$ light curves (data points) resulting from the re-processing of three different illumination light curves. The solid line shows a scaled version of the UV/X-ray continuum light curve that illuminates the debris, which in a) follows the SPH accretion rate; b) decays with time as $t^{-5/3}$; c) is constant. Note that the vertical axis is calibrated logarithmically in (a), while in (b) and (c) they have the same linear scale. The $\text{H}\alpha$ light curves rise initially as the illumination front propagates through the debris and then decay faster than the UV/X-ray light curves. The details of the calculation are described in §4.1.

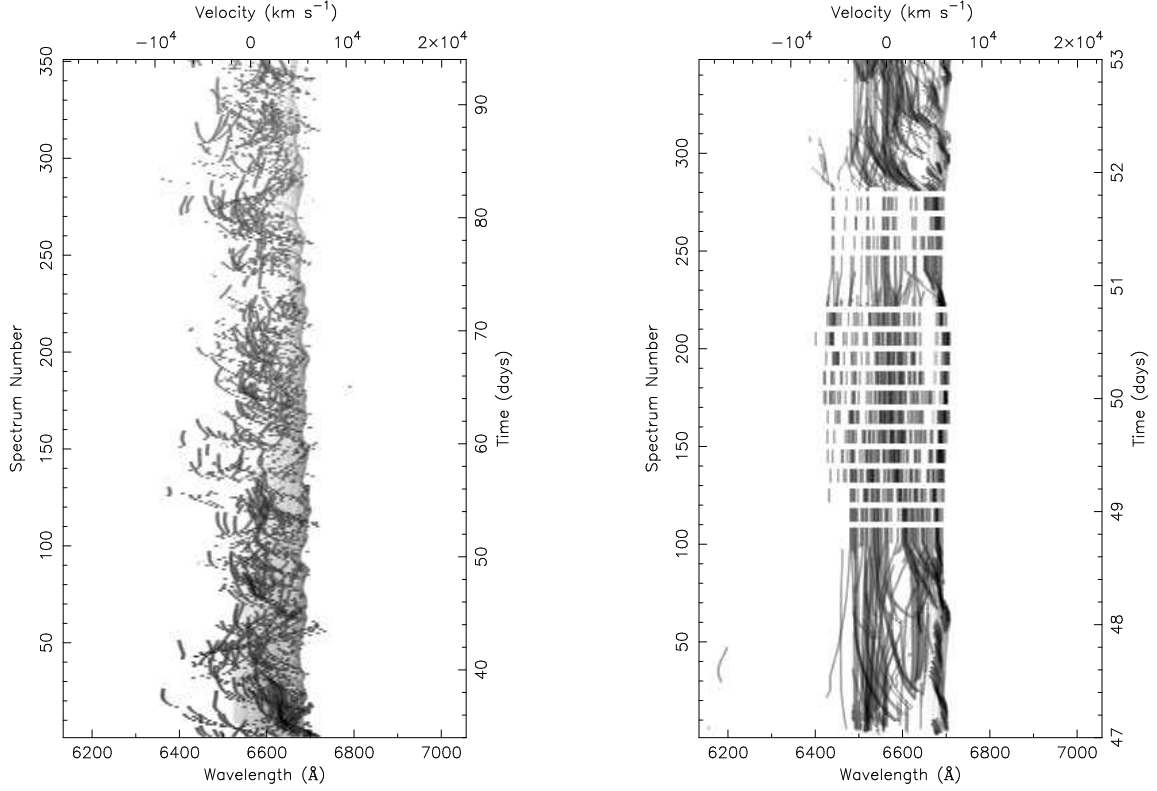


FIG. 5.— Trailed spectrogram of the simulated $H\alpha$ emission-line profiles from the 5k simulation spanning 60 days (left) and from the 20k simulation spanning 6 days (right). This is effectively a 2-dimensional intensity map versus projected velocity of the emitting material and time. Darker shades correspond to higher intensity. The scale on the right represents time since the tidal disruption event.

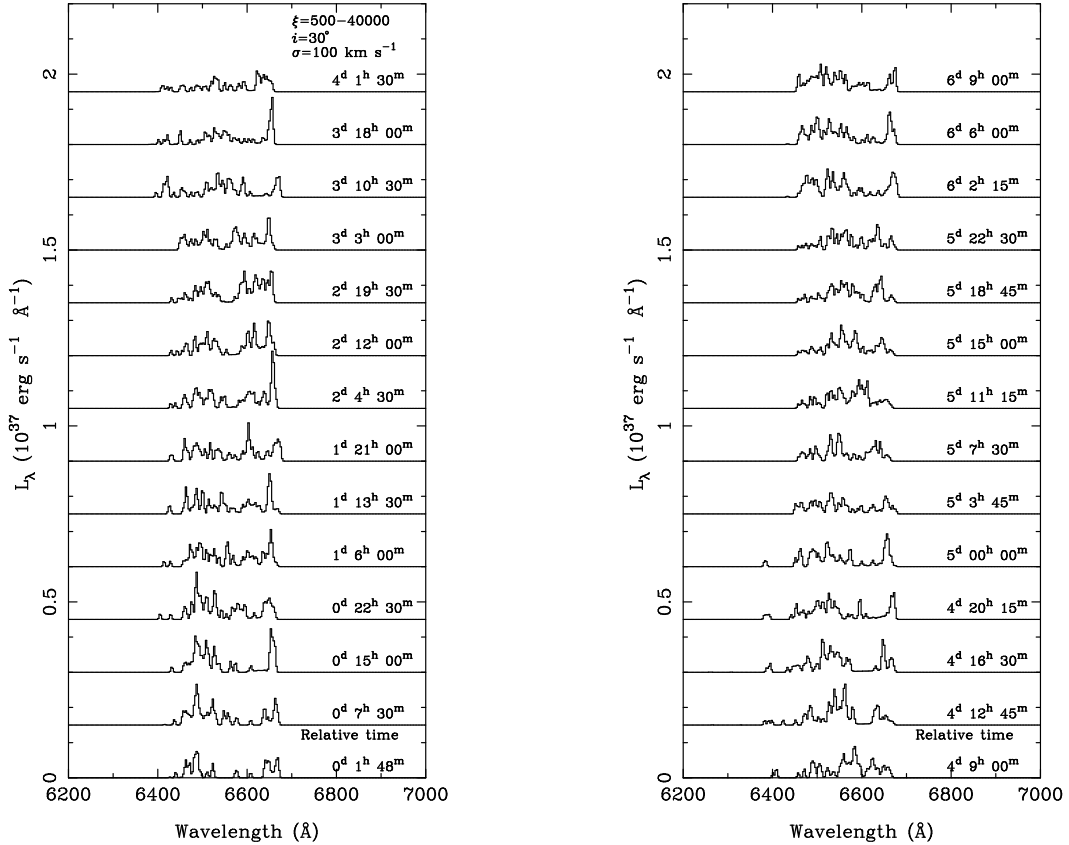


FIG. 6.— Sequence of $H\alpha$ profiles emitted from the region $\xi \in (500, 40000)$ over period of 6 days (20k run). The relative time from the beginning of the accretion phase onto the black hole is marked next to each profile. The accretion phase begins 47 days after the tidal disruption. The inclination of the debris plane and the velocity shear are as marked on the figure.

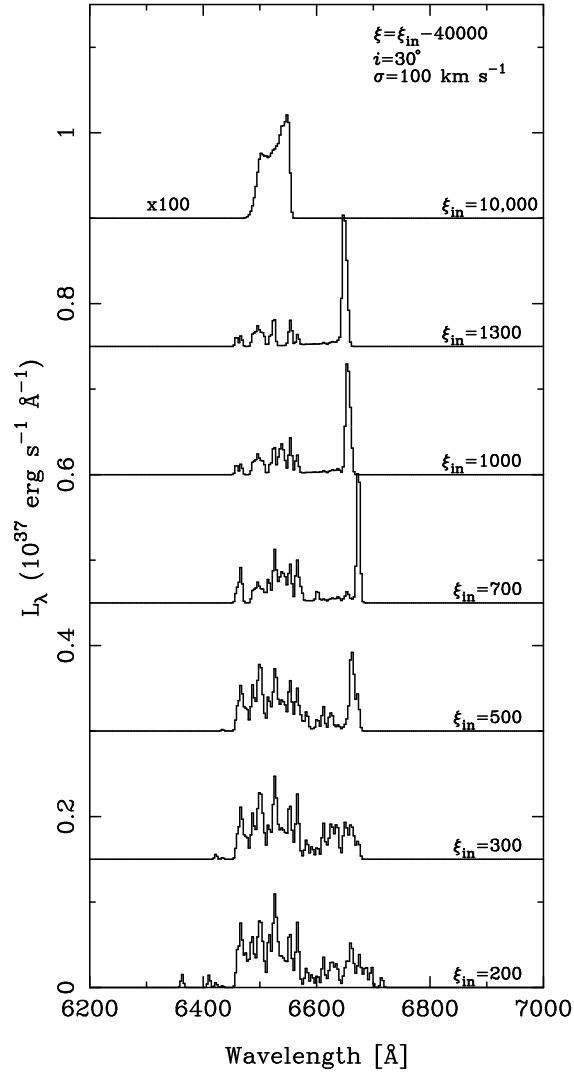


FIG. 7.— H α emission line profiles simulated for seven different values of inner radius (ξ_{in}), as determined by the propagation of the ionization front through the debris. The relative time for profile frames is $6^d 6^h 0^m$. The intensity of the profile calculated for $\xi_{in} = 10,000$ is multiplied by the factor of 100. The inclination and velocity shear are as marked on the top of the figure.

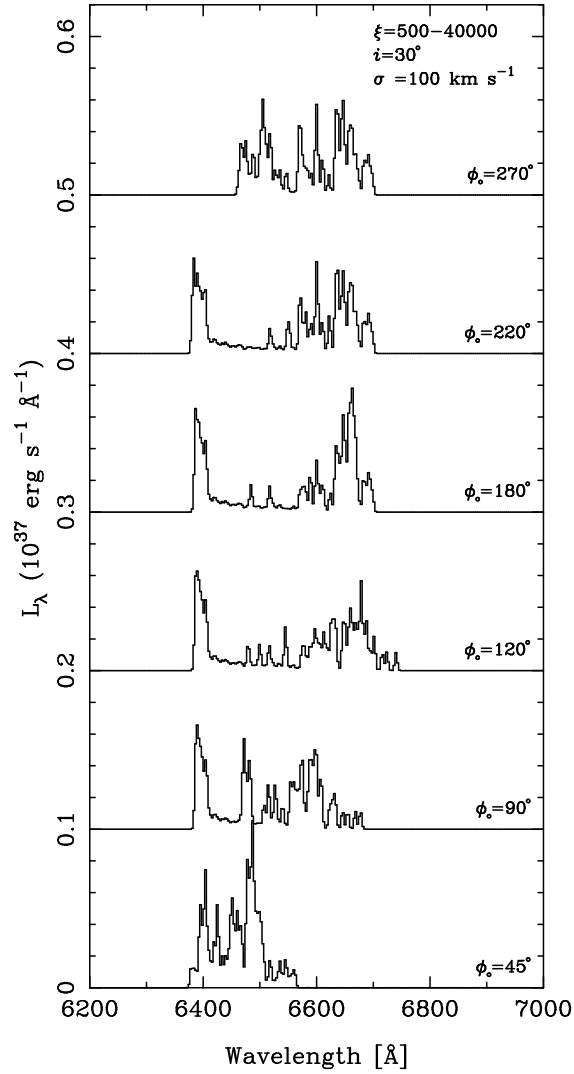


FIG. 8.— H α emission line profiles simulated for six different azimuthal orientations of the debris with respect to the observer, as represented by ϕ_0 . See profile in Figure 6 with the time label $5^d 22^h 30^m$ for orientation $\phi_0 = 0^\circ$. The size of the emitting region, inclination and velocity shear are as marked on the top of the figure.

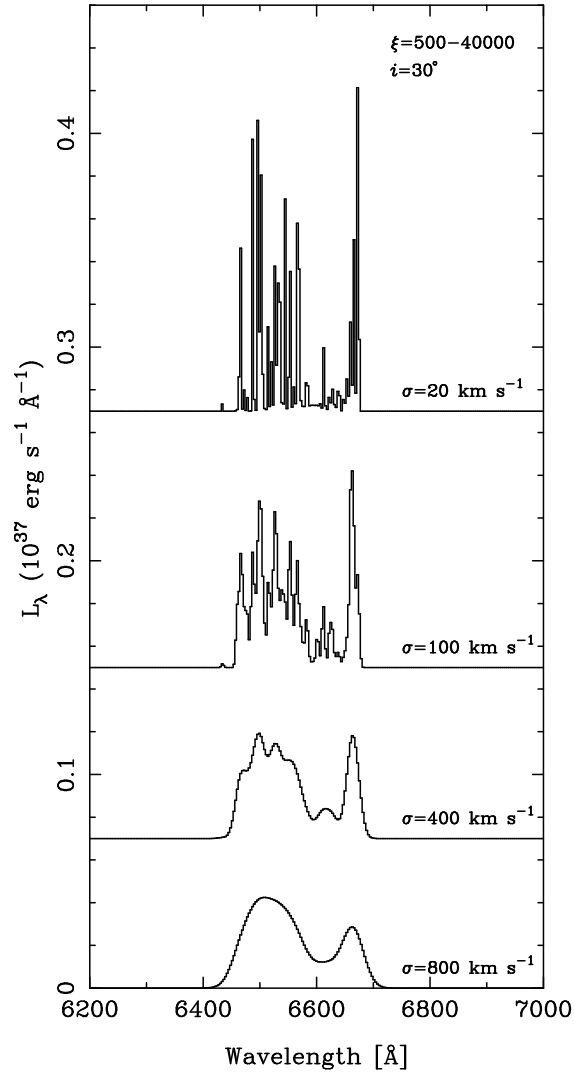


FIG. 9.— H α emission line profiles simulated for four different values of velocity dispersion. A velocity dispersion of 100 km s $^{-1}$ is the equivalent of an instrumental resolution of 2 Å. The relative time for the profile frames is $6^d 6^h 0^m$. Size of the emitting region and inclination are as marked on the top of the figure.